ELSEVIER

Volume 180, Number 2, February 2007

JOURNAL OF SOLID STATE CHEMISTRY

www.elsevier.com/locate/jssc

CONTENTS

Abstracted/indexed in BioEngineering Abstracts, Chemical Abstracts, Coal Abstracts, Current Contents/Physics, Chemical, & Earth Sciences, Engineering Index, Research Alert, SCISEARCH, Science Abstracts, and Science Citation Index. Also covered in the abstract and citation database SCOPUS®. Full text available on ScienceDirect®.

Regular Articles

Structural phase transitions and crystal chemistry of the series $Ba_2LnB'O_6$ (Ln = lanthanide and B' = Nb^{5+} or Sb^{5+})

Paul J. Saines, Brendan J. Kennedy and Margaret M. Elcombe

Page 401

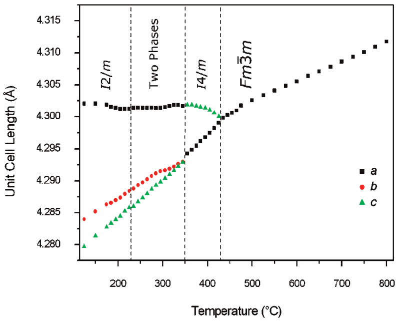

Lattice parameters versus temperature for Ba_2NdNbO_6. The formation of the $I4/m$ tetragonal phase contrasts with the antimonate series where a rhombohedral structure occurs instead. This difference is believed to be caused by the presence of π-bonding present in the niobates but absent in the antimonates.

Crystal structure and phonon properties of noncentrosymmetric $LiNaB_4O_7$

M. Mączka, A. Waśkowska, A. Majchrowski, J. Żmija, J. Hanuza, G.A. Peterson and D.A. Keszler

Page 410

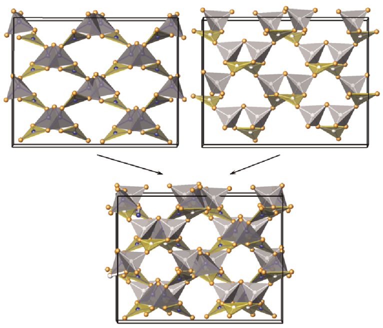

Structure of $LiNaB_4O_7$ borate showing two independent B_4O_7 frameworks and their interpenetration.

Regular Articles—Continued

Local structure and influence of bonding on the phase-change behavior of the chalcogenide compounds $K_{1-x}Rb_xSb_5S_8$

J.B. Wachter, K. Chrissafis, V. Petkov, C.D. Malliakas, D. Bilc, Th. Kyratsi, K.M. Paraskevopoulos, S.D. Mahanti, T. Torbrügge, H. Eckert and M.G. Kanatzidis

Page 420

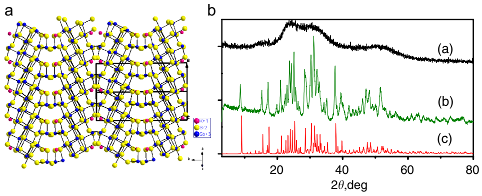

The KSb_5S_8 is a good example of a phase-change material with a mixed ionic/covalent bonding. The members of the $K_{1-x}Rb_xSb_5S_8$ series exhibit phase-change properties with greater glass forming ability (GFA) than KSb_5S_8. The GFA increases with increasing Rb content. In this case, the random alloy disorder in the alkali metal sublattice seems to predominate over the increased degree of ionicity in going from K···S to Rb···S bonding and works to stabilize the glass forms in $K_{1-x}Rb_xSb_5S_8$.

Synthesis and single crystal structures of ternary phosphides Li_4SrP_2 and $AAeP$ (A = Li, Na; Ae = Sr, Ba)

Yongkwan Dong and Francis J. DiSalvo

Page 432

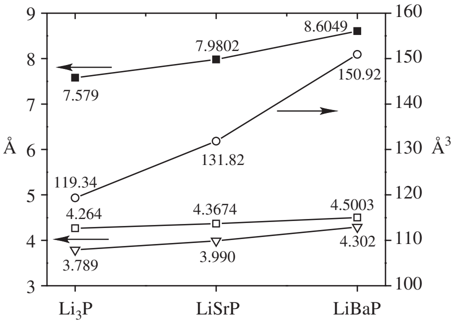

Comparison of the unit cell parameters and anionic interlayer distances between Li_3P and $LiAeP$ (Ae = Sr, Ba). (□: a-axis, ■: c-axis, ○: unit cell volume, ▽: interlayer distance).

Continued

Metal valences in electron-doped $(Sr,La)_2FeTaO_6$ double perovskite: A ^{57}Fe Mössbauer spectroscopy study

E.-L. Rautama, J. Lindén, H. Yamauchi and
M. Karppinen

Page 440

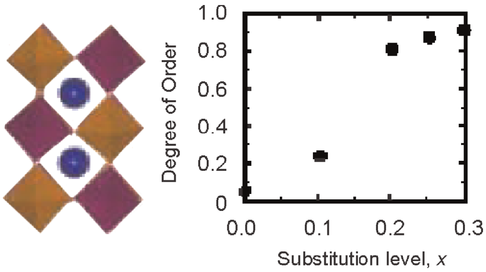

Both the degree of order and the valence states of Fe and Ta are controlled in the $(Sr_{1-x}La_x)_2FeTaO_6$ double perovskite oxide through aliovalent La^{III}-for-Sr^{II} substitution.

Hydrothermal synthesis, crystal structure, and characterization of a new pseudo-two-dimensional uranyl oxyfluoride, $[N(C_2H_5)_4]_2[(UO_2)_4(OH_2)_3F_{10}]$

Kang Min Ok and Dermot O'Hare

Page 446

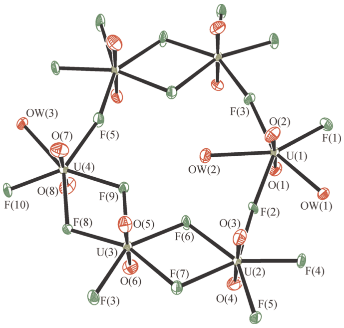

ORTEP (50% probability ellipsoids) drawing of $[N(C_2H_5)_4]_2$ $[(UO_2)_4(OH_2)_3F_{10}]$ in the *ab*-plane. Note the pentagonal bipyramidal environments of U^{6+} cations to form a novel six-membered ring.

Habit modification of calcium carbonate in the presence of malic acid

Zhaofeng Mao and Jianhua Huang

Page 453

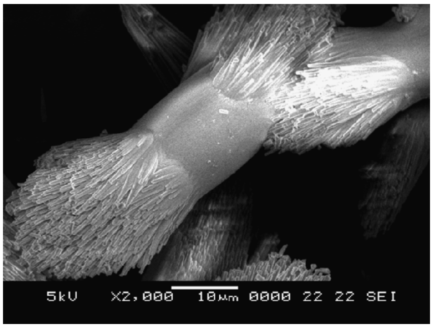

Dumbbell-like $CaCO_3$ particles obtained in the presence of malic acid.

High-yield synthesis and characterization of monodisperse sub-microsized $CoFe_2O_4$ octahedra

Xian-Ming Liu, Shao-Yun Fu and Lu-Ping Zhu

Page 461

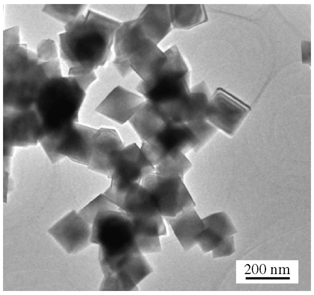

TEM image of $CoFe_2O_4$ octahedra

Sub-micro-sized $CoFe_2O_4$ octahedra with a high yield are synthesized via a simple hydrothermal route under mild conditions. TEM image shows that the edge size of $CoFe_2O_4$ octahedra is estimated to be about 0.10–0.14 µm.

Energy transfer and heat-treatment effect of photoluminescence in Eu^{3+}-doped $TbPO_4$ nanowires

Weihua Di, Xiaojun Wang, Peifeng Zhu and
Baojiu Chen

Page 467

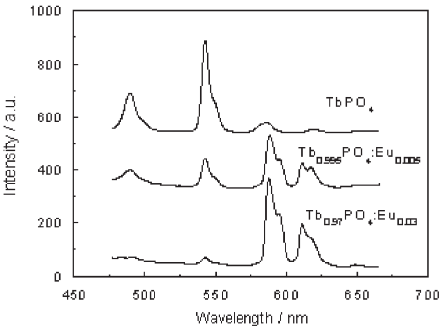

The energy transfer from Tb^{3+} to Eu^{3+} occurs in the Eu-doped $TbPO_4$ nanowires synthesized by the hydrothermal route.

Structural and magnetic study of the cation-ordered perovskites $Ba_{2-x}Sr_xErMoO_6$

Edmund J. Cussen

Page 474

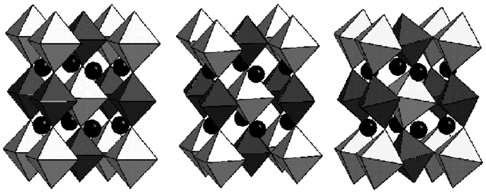

Introduction of Sr^{2+} into the double perovskite Ba_2ErMoO_6 introduces increasingly large distortions from cubic symmetry and permits antiferromagnetic order at $T_N \leqslant 4\,K$.

The effect of B_2O_3 addition on the crystallization of amorphous TiO_2–ZrO_2 mixed oxide

Dongsen Mao and Guanzhong Lu

Page 484

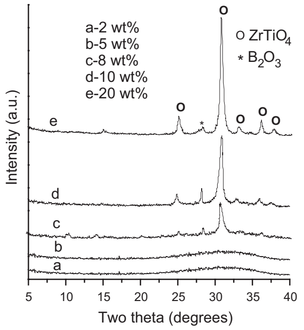

The addition of small amount of boria (<8 wt%) hinders the crystallization of amorphous TiO_2–ZrO_2 into a crystalline $ZrTiO_4$ compound, while the larger amount of boria (⩾8 wt%) promotes the crystallization process.

Template free fabrication of hollow hematite spheres via a one-pot polyoxometalate-assisted hydrolysis process

Baodong Mao, Zhenhui Kang, Enbo Wang, Chungui Tian, Zhiming Zhang, Chunlei Wang, Yanli Song and Meiye Li

Page 489

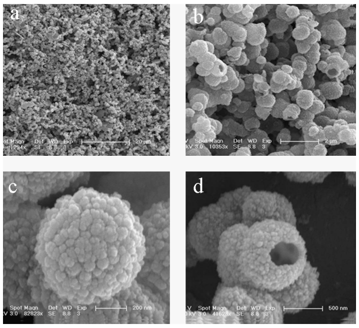

Uniform hollow hematite (α-Fe_2O_3) spheres with diameter of about 600–700 nm and shell thickness lower than 100 nm are obtained by direct hydrothermal treatment of dilute $FeCl_3$ and tungstophosphoric acid $H_3PW_{12}O_{40}$ solution at 180 °C. The hollow spheres present a high surface area and weak ferromagnetic behavior at room temperature.

The Pr_2Se_3–$PrSe_2$ system: Studies of the phase relationships and the modulated crystal structure of $PrSe_{1.85}$

Thomas Doert, Christian Graf, Peer Schmidt, Inga G. Vasilieva, Paul Simon and Wilder Carrillo-Cabrera

Page 496

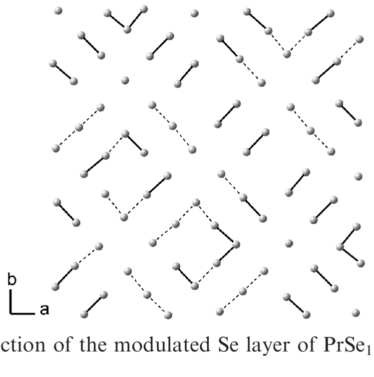

Section of the modulated Se layer of $PrSe_{1.85}$.

High-pressure phase transition in $LiBH_4$

A.V. Talyzin, O. Andersson, B. Sundqvist, A. Kurnosov and L. Dubrovinsky

Page 510

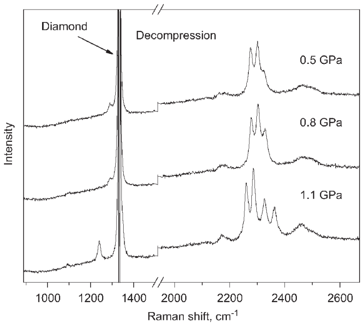

Raman spectra of $LiBH_4$ in the region of the phase transition recorded during decompression.

Structure characterization of 1:1 adducts of metal(II) halides and piperazine

Jie-Hui Yu, Qin Hou, Tie-Gang Wang, Xiao Zhang and Ji-Qing Xu

Page 518

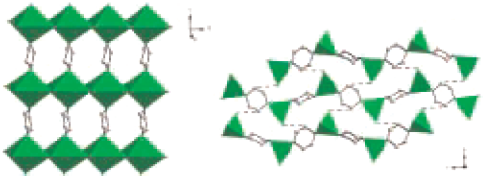

Two 1:1 adducts of MX_2 and piperazine (pip), $[CdI_2(pip)]$ **1** and $[CoCl_2(pip)]$ **2**, were prepared by the simple hydro/solvothermal techniques. With pip as the bridges, the 1-D linear CdI_2 chains are extended into a 2-D layered compound **1**, while the mononuclear $CoCl_2$ units are linked into a 1-D zigzag-type chain compound **2**. Compound **1** possesses the fluorescence property with the emission peaks at 373 nm and 410 nm.

Thermodynamic studies on $SrFe_{12}O_{19}(s)$, $SrFe_2O_4(s)$, $Sr_2Fe_2O_5(s)$ and $Sr_3Fe_2O_6(s)$

S.K. Rakshit, S.C. Parida, S. Dash, Z. Singh, B.K. Sen and V. Venugopal

Page 523

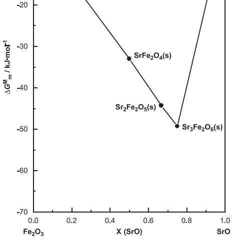

Gibbs energy of mixing of ternary oxides of the system Sr–Fe–O.

Continued

Chemical bonding in Eu*T*Ge (*T* = Ni, Pd, Pt) and physical properties of EuPdGe

Xavier Rocquefelte, Régis Gautier, Jean-François Halet, Ralf Müllmann, Carsten Rosenhahn, Bernd D. Mosel, Gunter Kotzyba and Rainer Pöttgen

Page 533

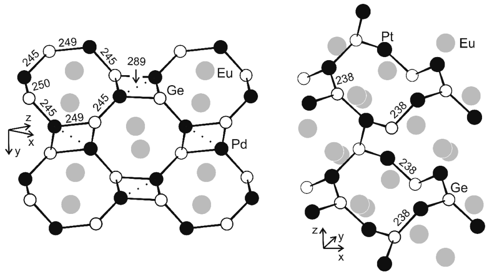

EuPdGe EuPtGe

Cutouts of the [PdGe] and [PtGe] polyanions in the structures of EuPdGe and EuPtGe. Atom designations and some relevant interatomic distances are given.

Composition and temperature dependent phase transitions in Co–W double perovskites, a synchrotron X-ray and neutron powder diffraction study

Qingdi Zhou, Brendan J. Kennedy and Margaret M. Elcombe

Page 541

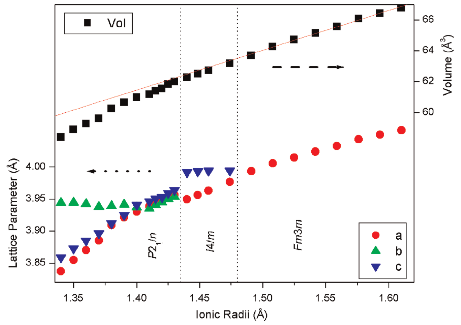

Variation of the reduced lattice parameters and volumes with the average A cation radius for the series $A_{2-x}Sr_xCoWO_6$. The reduced lattice parameters are, for $P2_1/n$ $a' = \sqrt{2}a_p$, $b' = \sqrt{2}b_p$, $c' = 2c_p$ for $I4/m$, $a' = \sqrt{2}a_p$, $c' = 2c_p$ and for $Fm\bar{3}m$ $a' = 2a_p$.

The local crystal chemistry and dielectric properties of the cubic pyrochlore phase in the Bi_2O_3–M^{2+}O–Nb_2O_5 ($M^{2+} = Ni^{2+}$ and Mg^{2+}) systems

Binh Nguyen, Yun Liu and Ray L. Withers

Page 549

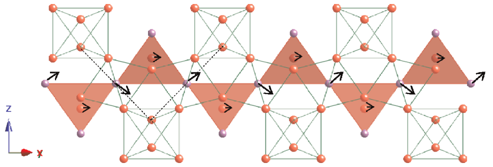

The characteristic *β*-cristobalite-type displacive disorder of the O'A_2 sub-structure (of the ideal pyrochlore structure type) drawn relative to the surrounding B_2O_6 octahedral framework sub-structure and responsible for the observed structured diffuse intensity distribution in the $Bi_{1.65}Ni_{0.75}Nb_{1.50}O_7$ and $Bi_{1.67}Mg_{0.64}Nb_{1.53}O_7$ misplaced-displacive cubic pyrochlores.

A novel nanomolecular organic–inorganic hybrid compound: $Na_2[NH(CH_2CH_2OH)_3]_4\{Mo_{36}O_{112}(OH_2)_{14}[OHCH_2CH_2NH(CH_2CH_2OH)_2]_2\} \cdot nH_2O$ ($n \approx 72$) exhibiting a supramolecular one-dimensional chainlike structure

Da-Dong Liang, Shu-Xia Liu, Chun-Ling Wang and Yuan-Hang Ren

Page 558

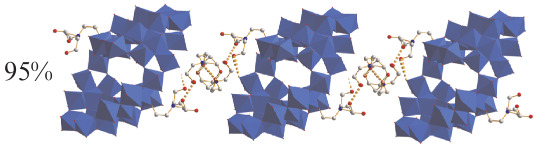

A novel organic–inorganic hybrid material based on macroisopolyanion $\{Mo_{36}\}$ has been synthesized and characterized by X-ray single-crystal crystallography, XRD, IR spectroscopy, and TG analysis. The material exhibits a supramolecular one-dimensional chainlike structure. The $\{Mo_{36}(TEAH^+)_2\}$ unit could be considered as nanosized chelating ligand with [2N, 4O] donor sets.

Mesoporous aluminosilicate ropes with improved stability from protozeolitic nanoclusters

Junlin Zheng, Dejin Kong, Weimin Yang, Zaiku Xie, Dong Wu and Yuhan Sun

Page 564

Mesoporous aluminosilicate ropes with enhanced hydrothermal stability were fabricated from protozeolitic nanoclusters through $S^+X^-I^+$ route in HNO_3 solution under the direction of CTAB templates.

Structural change of layered perovskite $La_2Ti_2O_7$ at high pressures

F.X. Zhang, J. Lian, U. Becker, R.C. Ewing, L.M. Wang, Jingzhu Hu and S.K. Saxena

Page 571

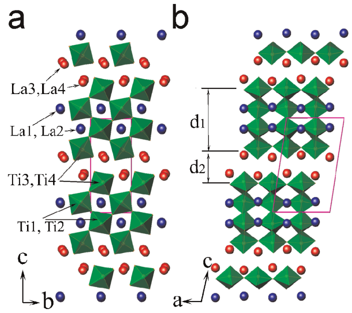

$La_2Ti_2O_7$ is a layered perovskite and it shows anisotropic compressibility at high pressures. The in situ XRD and Raman measurements indicate a structural transformation takes place at 16.7 GPa.

Low-alkali metal content in β-vanadium mixed bronzes: The crystal structures of β-$K_x(V,Mo)_6O_{15}$ ($x = 0.23$ and 0.32) by single-crystal X-ray diffraction

Michele Zema, Paolo Ghigna and Serena C. Tarantino

Page 577

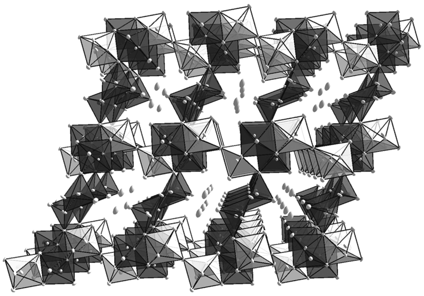

Perspective view of the crystal structure of $K_xV_{6-y}Mo_yO_{15}$ along [010]. This vanadium-molybdenum mixed bronze assumes the β-$Na_xV_6O_{15}$ (bannermanite-type) structure, in which Mo(VI) substitutes for V only in the V2 position. The alkali metal content in the studied crystals is much lower than the solubility limit found for the analogous Na containing compounds.

Construction of a double-layered tetrahedral network within a perovskite host: Two-step route to the alkali-metal-halide layered perovskite, $(Li_xCl)LaNb_2O_7$

Liliana Viciu, Thomas A. Kodenkandath and John B. Wiley

Page 583

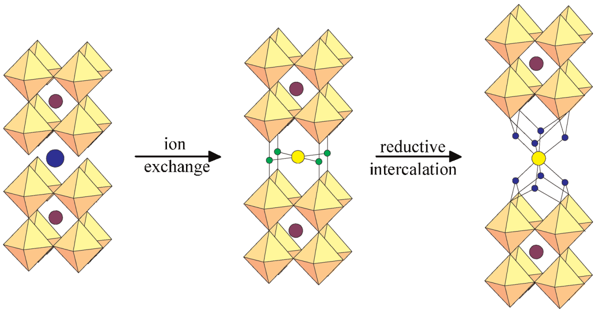

Alkali-halide layers can be constructed within a layered perovskite host via a two-step topochemical process.

The relationship between the thermal expansions and structures of ABO_4 oxides

Huiling Li, Shihong Zhou and Siyuan Zhang

Page 589

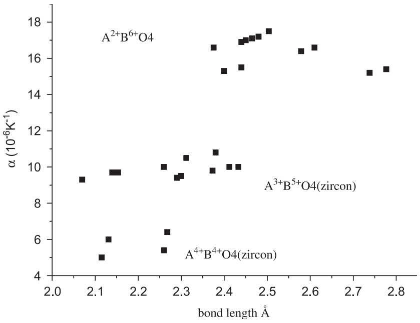

The evaluated CTEs of *A*-O bonds change against *A*-O bond distances.

Preparation, crystal structure and thermal expansion of a new bismuth barium borate, $BaBi_2B_4O_{10}$

R.S. Bubnova, S.V. Krivovichev, S.K. Filatov, A.V. Egorysheva and Y.F. Kargin

Page 596

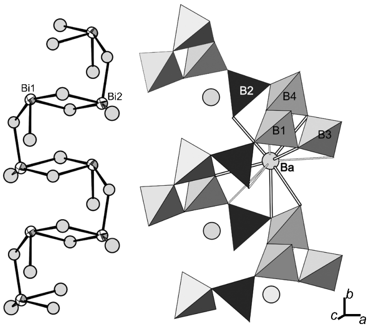

New borate and bismuthate one-dimensional polyions.

Magnetic properties of $DyCo_5$ and $TbCo_5$ intermetallics from the electronic structure calculations

G.I. Miletić and Ž. Blažina

Page 604

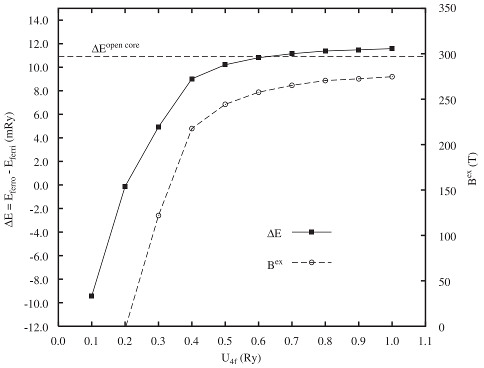

Differences between total energies of ferromagnetic and ferrimagnetic configurations in $DyCo_5$ together with the corresponding exchange fields vs. the U_{4f} parameter.

A sol–gel route for the development of rare-earth aluminum borate nanopowders and transparent thin films

Lauro J.Q. Maia, Valmor R. Mastelaro, Sebastien Pairis, Antonio C. Hernandes and Alain Ibanez

Page 611

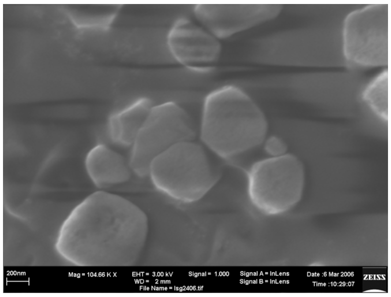

SEM micrograph of $Y_{0.9}Er_{0.1}Al_3(BO_3)_4$ powders calcined at 400 and 700 °C during 24 h and heat-treated at 1150 °C.

Continued

Structural, spectroscopic and photoluminescence studies of LiEu$(WO_4)_{2-x}(MoO_4)_x$ as a near-UV convertible phosphor

Chuang-Hung Chiu, Ming-Fang Wang, Chi-Shen Lee and Teng-Ming Chen

Page 619

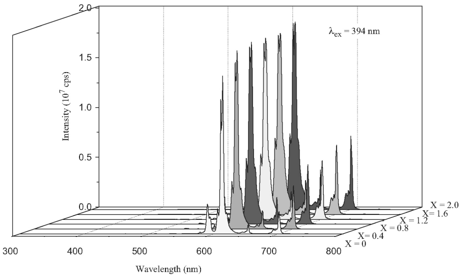

As shown by the PL spectra of LiEu$(WO_4)_{2-x}(MoO_4)_x$ ($x = 0$, 0.4, 0.8, 1.2, 1.6, 2.0) under 394 nm near-UV excitation, the intensity of $^5D_0 \rightarrow {}^7F_2$ transition was found to increase with the increasing x and the I–λ curve reaches a maximum when the relative ratio of Mo/W is 2:0.

Structure and magnetism of rare-earth-substituted $Ca_3Co_2O_6$

Charles H. Hervoches, Helmer Fjellvåg, Arne Kjekshus, Vivian Miksch Fredenborg and Bjørn C. Hauback

Page 628

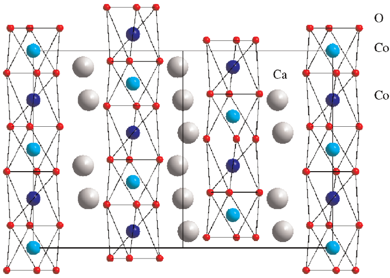

Yttrium- and rare-earth-substituted derivatives of $Ca_{3-v}R_vCo_2O_6$ have been synthesized. A significant increase in the Co2–O distances within the trigonal-prismatic Co_2O_6 coordination polyhedra confirms that extra electrons from the R^{3+}-for-Ca^{2+} substitution enter the Co2 site, thereby formally reducing its valence state. The long-range ferrimagnetic ordering of the parent $Ca_3Co_2O_6$ phase vanishes at $v > {\sim}0.30$ in $Ca_{3-v}R_vCo_2O_6$.

Ternary rare earth and actinoid transition metal carbides viewed as carbometalates

Enkhtsetseg Dashjav, Guido Kreiner, Walter Schnelle, Frank R. Wagner, Rüdiger Kniep and Wolfgang Jeitschko

Page 636

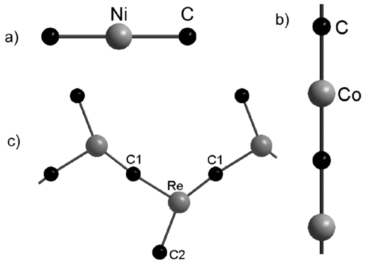

Carbometalates represent a specific class of ternary carbides whose crystal structures contain complex anions, e.g., (a) discrete complex anion $[NiC_2]^{8-}$ in the crystal structure of Th_2NiC_2, (b) $^1_\infty[(CoC)^{3-}]$ linear chain in the crystal structure of YCoC, (c) $^1_\infty[(ReC_2)^{6-}]$ zigzag chain in Pr_2ReC_2.

Carbon nanotube assisted synthesis of CeO_2 nanotubes

Dengsong Zhang, Hongxia Fu, Liyi Shi, Jianhui Fang and Qiang Li

Page 654

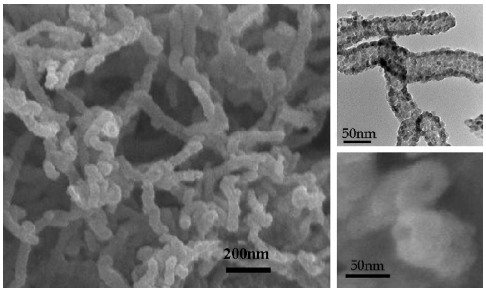

CeO_2 nanotubes have been synthesized facilely using carbon nanotubes as templates by a liquid phase deposition method. The obtained CeO_2 nanotubes are composed of many tiny interconnected nanocrystallites of about 10 nm in size, and have a uniform diameter ranging from 40 to 50 nm.

$Bi_{2n+4}Mo_nO_{6(n+1)}$ with $n = 3, 4, 5, 6$: A new series of low-temperature stable phases in the $mBi_2O_3-MoO_3$ system $(1.0 < m < 1.7)$: Structural relationships and conductor properties

Eladio Vila, Ángel R. Landa-Canovas, Jean Galy, Juan E. Iglesias and Alicia Castro

Page 661

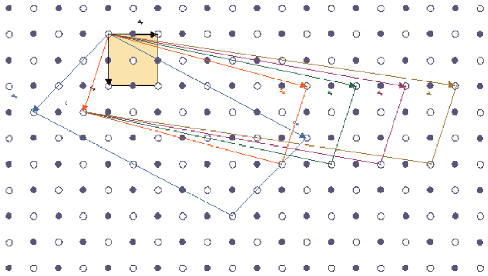

Four new phases $Bi_{10}Mo_3O_{24}$, $Bi_6Mo_2O_{15}$, $Bi_{14}Mo_5O_{36}$ and $Bi_8Mo_3O_{21}$ have been synthesized, characterized and described as consecutive members of a new family $Bi_{2n+4}Mo_nO_{6(n+1)}$, with $n = 3$, 4, 5 and 6. They are based on basic fluorite-type structure and their unit cells are depicted in the accompanying graphic.

Titanium vacancy defects in sol–gel prepared anatase

Ian.E. Grey and Nicholas C. Wilson

Page 670

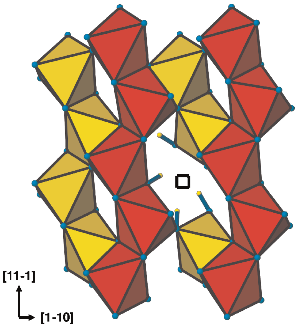

Relaxed structure from DFT modelling of anatase containing one titanium vacancy and four protons.

Synthesis and characterization of $Ti_{1-2x}Nb_xNi_xO_{2-x/2}$ solid solutions

Mónica Martos, Beatriz Julián, Hakim Dehouli, Didier Gourier, Eloisa Cordoncillo and Purificación Escribano

Page 679

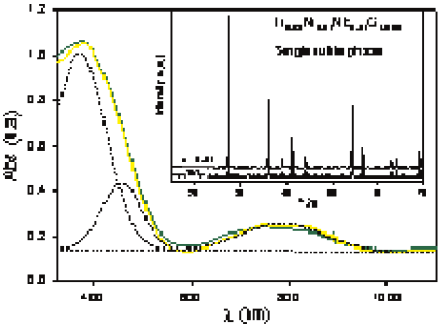

The synthesis and characterization of the $Ti_{1-2x}Nb_xNi_xO_{2-x/2}$ system prepared by traditional solid-state and sol–gel methodologies is reported. The incorporation of the doping ions in the rutile structure by Rietveld refinements and the magnetic response are discussed. The similarity found by both procedures introduces new possibilities of coloured TiO_2-based solid solutions.

On the relaxation/transformation of NiO-dissolved TiO_2 condensates with fluorite-type derived structures

Chang-Ning Huang, Pouyan Shen and Shuei-Yuan Chen

Page 688

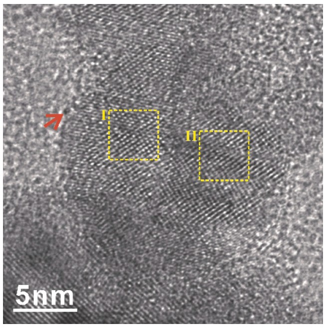

Lattice image of NiO-dissolved TiO_2 condensate having local fluorite-type (region I) and baddeleyite-type (region II) structures and (010) facet (arrow).

Hydrophilic and hydrophobic nano-sized Mn_3O_4 particles

Pierre Gibot and Lydia Laffont

Page 695

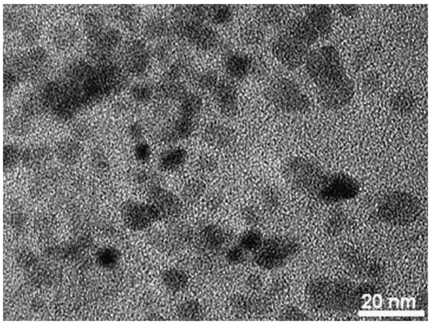

Hydrophobic nano-sized Mn_3O_4 particles.

Quantum chemical and spectroscopic analysis of calcium hydroxyapatite and related materials

V.D. Khavryuchenko, O.V. Khavryuchenko and V.V. Lisnyak

Page 702

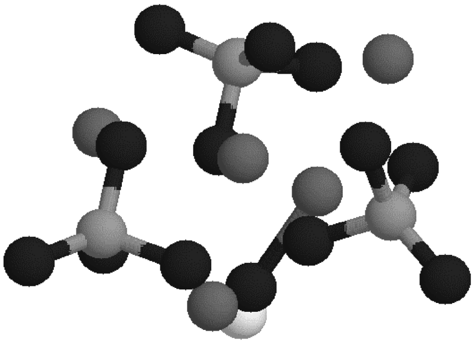

The structure of the quantum chemically optimized $Ca_5(PO_4)_3(OH)$ cluster, which was used for vibrations spectra simulation.

Hydrothermal synthesis, structure and thermal stability of diamine templated layered uranyl-vanadates

Murielle Rivenet, Nicolas Vigier, Pascal Roussel and Francis Abraham

Page 713

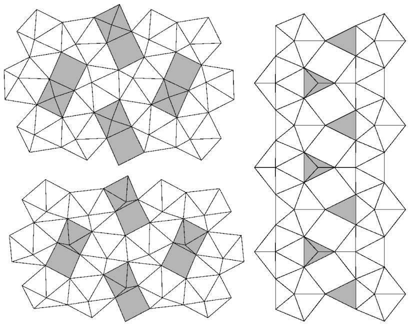

The three types of layer in layered uranyl-vanadates using diamine as a structure-directing agent.

Preparation and visible-light photocatalytic activity of Ag_3VO_4 powders

Xuexiang Hu and Chun Hu

Page 725

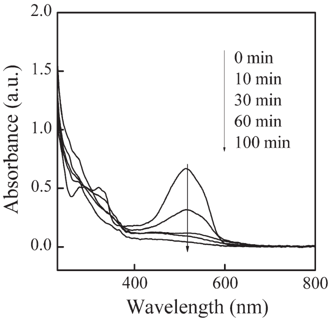

The UV/vis spectral changes of ARB solution recorded for NiO/Ag_3VO_4 as a function of irradiation time.

Continued

Crystal chemistry of the G-phases in the {Ti, Zr, Hf}–Ni–Si systems

A. Grytsiv, Xing-Qiu Chen, P. Rogl, R. Podloucky, H. Schmidt, G. Giester and V. Pomjakushin

Page 733

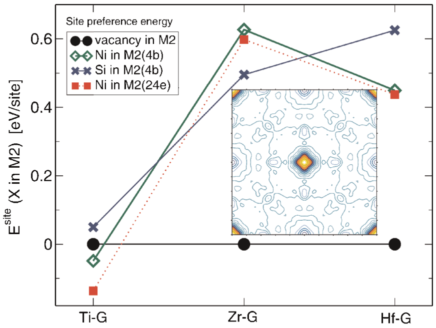

$Ti_6Ni_{16.7}Si_7$ (G-Phase, Ti-G) was found to crystallize in a new variant of the filled Th_6Mn_{23}-type structure with an additional Ni atom partially occupying the 24*e* site inside Ti octahedra, where Ti atoms occupy a split position.

High-pressure synthesis, crystal structure, and properties of the first ternary hafniumborate β-HfB_2O_5

Johanna S. Knyrim and Hubert Huppertz

Page 742

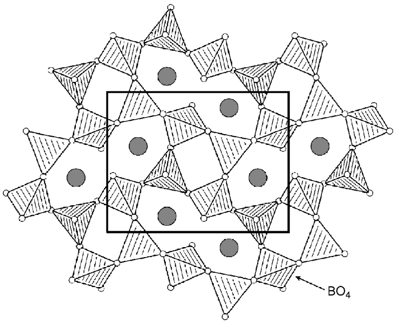

Synthesis of β-HfB_2O_5 via the multianvil high-pressure/high-temperature technique, representing the first ternary compound in the borate system Hf–B–O.

Structural study of VO_x doped aluminium fluoride and aluminium oxide catalysts

Kerstin Scheurell, Gudrun Scholz and Erhard Kemnitz

Page 749

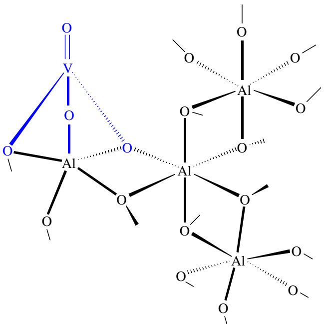

Structure model for VO_x doped aluminium oxide.

Synthesis, structure, optical properties, and electronic structure of $NaLiCdS_2$

Bin Deng, George H. Chan, Fu Qiang Huang, Danielle L. Gray, Donald E. Ellis, Richard P. Van Duyne and James A. Ibers

Page 759

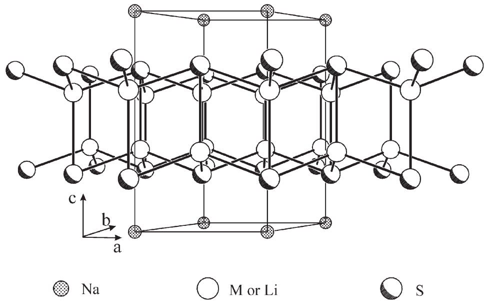

Crystal structure of NaLi*M*S (*M* = Cd, Zn).

Charge transport properties in microcrystalline $KDyFe(CN)_6$

P.H. Aubert, F. Goubard, C. Chevrot and A. Tabuteau

Page 765

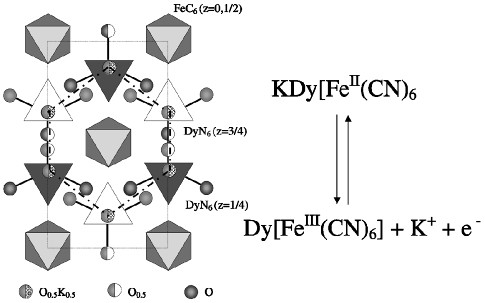

Dy and Fe polyhedra packing in the cell of $KDyFe(CN)_6 \cdot 3.5H_2O$ shows occluded water molecules and potassium ions forming a pseudo-hexagonal 2D sub-lattice connected to each other by diffusion channels.

Synthesis, structure, and physicochemical investigations of the new α $Cu_{0.50}TiO(PO_4)$ oxyphosphate

S. Benmokhtar, H. Belmal, A. El Jazouli, J.P. Chaminade, P. Gravereau, S. Pechev, J.C. Grenier, G. Villeneuve and D. de Waal

Page 772

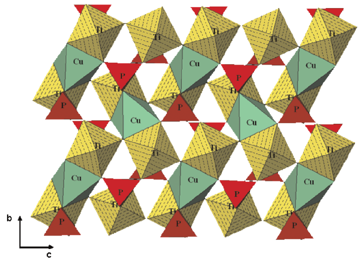

Projection of the structure of α $Cu_{0.50}TiO(PO_4)$ along the *a*-axis.

Fabrication of MCM-41 mesoporous silica through the self-assembly supermolecule of *β*-CD and CTAB

Zhaodong Nan, Xia Xue, Wanguo Hou, Xin Yan and Shuhua Han

Page 780

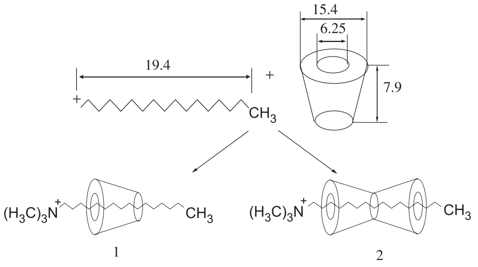

1:1 and 1:2 complexes between CTAB and *β*-CD have formed as self-assembly templates in the formation of MCM-41.

The structure and ordering of zirconium and hafnium containing garnets studied by electron channelling, neutron diffraction and Mössbauer spectroscopy

Karl R. Whittle, Gregory R. Lumpkin, Frank J. Berry, Gordon Oates, Katherine L. Smith, Sergey Yudintsev and Nestor J. Zaluzec

Page 785

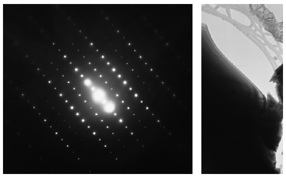

Dynamical diffraction pattern for kimzeyite along the 3 1 1 direction, used in the electron channelling analysis, and a bright field image of the sample investigated, the magnification is 25 000.

Rapid Communications

Synthesis, characterization, and electrochemical properties of ordered mesoporous carbons containing nickel oxide nanoparticles using sucrose and nickel acetate in a silica template

Yulin Cao, Jieming Cao, Mingbo Zheng, Jinsong Liu and Guangbin Ji

Page 792

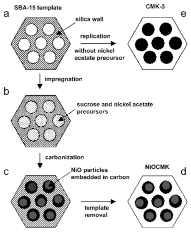

Schematic drawings of synthesis routes for the NiOCMK materials.

Ionic liquid of $[\text{Bmim}]^+\text{Cl}^-$ for the preparation of hierarchical nanostructured rutile titania

Ningya Yu, Liming Gong, Huijuan Song, Yong Liu and Donghong Yin

Page 799

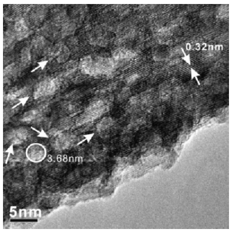

Ionic liquid of $[\text{Bmim}]^+\text{Cl}^-$ was employed to prepare rutile titania with hierarchical nanostructure, in which the nanorods were interaggregated to fabricate a large mesoporous structure and the voids packed in the nanorods formed a small mesostructure.